Optical parameters extraction of zinc oxide thin films doped with manganese using an innovative technique based on the dragonfly algorithm and their correlation to the structural properties

K. Settara[a,b,*], F. Lekoui[c], H. Akkari[d], E. Garoudja[e], R. Amrani[f], W. Filali[e],
S. Oussalah[g], S. Hassani[c]
[a]*Laboratory of Research on Physico-Chemistry of Surface and Interface (LRPCSI), University of 20 August 1955 Skikda, BP 26, Road El Hadaiek, Skikda, 21000, Algeria*
[b]*Laboratory of Mechanical and Materials Engineering (LGMM), University of 20 August 1955 Skikda, BP 26, Road El Hadaiek, Skikda, 21000, Algeria*
[c]*Ionized Media & Laser Division (IMLD), Center for Development of Advanced Technologies (CDTA), Cité 20 Août 1956, Baba Hassen, Algiers, 16081, Algeria*
[d]*Department of Industrial Engineering, Faculty of Technology, University Batna 2 Chahid Mostefa Ben Boulaid, Rue Chahid Boukhlouf M. El Hadi, Batna, 05001, Algeria*
[e]*Micro-manufacturing Technology Platform, Center for Development of Advanced Technologies (CDTA), Cité 20 Août 1956, Baba Hassen, Algiers, 16081, Algeria*
[f]*Department of Material Sciences, University of Algiers Ben Youssef Ben Khadda, 2 Rue Didouche Mourad, Algiers, 16000, Algeria*
[g]*Microelectronic & Nanotechnology Division, Center for Development of Advanced Technologies (CDTA), Cité 20 Août 1956, Baba Hassen, Algiers, 16081, Algeria*

Pure zinc oxide (ZnO) thin films, along with manganese (Mn) doped counterparts, were produced using rapid thermal evaporation technique on ordinary glass substrates. Post-annealing treatments resulted in the formation of hexagonal wurtzite structures in the deposited layers. The Raman results unveiled the presence of A1(LO) and LVM vibration modes in each sample that were doped. Interestingly, the undoped sample lacked the LVM mode while showcasing the emergence of LA + TO combined phonons. Employing a novel approach reliant on the Dragonfly Algorithm, optical parameters were extracted, revealing a drop in the bandgap energy of the films from 3.95 eV to 3.79 eV.

1. Introduction

Thanks to its properties such as wide bandgap (~3.37 eV), abundance on earth, non-toxicity, stability, and low cost, zinc oxide (ZnO) has become a promising candidate as a replacement to reduce the use of indium tin oxide (ITO) [1, 2] as well as titanium dioxide (TiO$_2$) [3] and stannic oxide (SnO$_2$) [4] in thin-film photovoltaic panels. Zinc oxide (ZnO) thin films possess transparency within the visible spectrum, rendering them suitable for applications like optical windows and solar cell electrodes [5-7]. Nevertheless, their conductivity tends to be weak due to their transparent nature. To address this limitation, doping with small percentages of transition metals like silver (Ag), aluminum (Al), iron (Fe), nickel (Ni), and manganese (Mn), among others, is commonly employed. This doping technique enhances electrical conductivity while preserving the transparency of the films.

Manganese (Mn) has been widely used as a metal for ZnO doping. Mn-doped ZnO (Mn:ZnO) films exhibit a significant homogeneity as a result of the strong ability of both materials to dissolve in each other [8]. The Mn^{2+} radii (0.80 Å) and Zn^{2+} (0.74 Å) are close, allowing Mn atoms to substitute Zn atoms easily. This behavior will alter the lattice parameters of ZnO without modifying the structure nature and subsequently cause changes in terms of physical properties, in particular the optical ones [9]. ZnO films can be synthesized on different substrates with several methods, such as pulsed laser deposition [10], sol-gel [11], spray pyrolysis [12, 13], chemical vapor deposition [14], magnetron sputtering [15-16], spin coating [17] and vacuum thermal evaporation [18].

This study examines the structural and optical features of Mn-doped ZnO thin films prepared via rapid thermal evaporation (RTE), focusing on the effect of Mn concentration. Structural properties were investigated using X-ray diffraction (XRD), Raman analysis, energy dispersive spectroscopy (EDS) analysis, and scanning electron microscopy (SEM). Optical characteristics were assessed through the optical transmission spectra obtained using an ultraviolet/visible/near-infrared (UV-Vis-NIR) spectrophotometer. Additionally, optical constants such as thickness, refractive index, extinction coefficient, and absorption coefficient were extracted from the transmission spectra using a novel approach based on the Dragonfly Algorithm (DA) [19], marking the first application of this technique in this context. The relationship between these optical constants and the Mn content will subsequently be studied.

In our previous works [8, 20], we succeeded in developing two methods of optical parameter extraction based on particle swarm optimization (PSO) and artificial bee colony (ABC) algorithm, respectively. Here, for the purpose of optimizing and enhancing research, we adopted a new technique that offers high efficiency in calculating the optical parameters of the deposited films, giving better results and understanding of the effect of doping. The novel method utilized in this study draws inspiration from the natural behaviors of dragonflies, known as the dragonfly algorithm. By emulating both the static and dynamic characteristics exhibited by dragonflies in their environment, this approach is employed to ascertain the optical parameters under investigation.

2. Experimental details

2.1. Preparing samples

Utilizing the rapid thermal evaporation (RTE) technique, both undoped and Mn-doped ZnO thin films were effectively fabricated on standard glass substrates, incorporating various weight percentages of the dopant (0, 5, 10, 15, and 20 wt.-%). High-purity ZnO and Mn powders sourced from Sigma-Aldrich (with a purity of 99.99%) were employed in the process. The substrate preparation involved a meticulous cleaning procedure, beginning with washing the glass substrates using distilled water and detergent. Subsequently, the substrates underwent a sequential immersion in an ultrasonic acetone bath for 5 minutes, followed by ethanol for an additional 5 minutes. The deposition technique was executed at a low pressure of 10^{-6} mbar by heating a crucible to a temperature of 1600 °C, at which the ZnO powder sublimates. The deposition was done quickly, lasting only 15 seconds. After being deposited, the films were subjected to air thermal annealing at a temperature of 500 °C for a period of 2 hours.

2.2. Characterization

The XRD technique was used to analyze the structure and morphology of the layers. This analysis was conducted by a Philips X'Pert-MPD diffractometer equipped with a Cu-Kα cathode source that emitted radiation with a wavelength of 1.54 Å. Raman spectroscopy recorded by Lab Ram H-Resolution and SEM coupled with EDX spectroscopy using a Hitachi S4800 cold field-emission. The optical characteristics were examined using a Shimadzu UV-1280 spectrophotometer.

2.3. Dragonfly algorithm

In 2016, an efficient optimization method known as the Dragonfly Algorithm was developed by S. Mirjalili [19]. It is chiefly originated from hunting and migrating behaviors of real dragonflies. Dragonfly hunting activity is referred to as static swarm, whereas migration behavior is referred to as dynamic swarm. In nature, dragonflies exhibit distinct behaviors depending on their context. In static swarms, they gather in small groups, navigating their surroundings in search of sustenance. Conversely, dynamic swarms involve a larger congregation of dragonflies migrating together in a unified direction. Analogously, in optimization algorithms, the exploration and exploitation stages closely resemble the behaviors observed in static and dynamic swarms, respectively. Every dragonfly represents a potential solution inside the search space. In this algorithm, six weights are employed to steer the dragonflies to their destinations: separation weight (s), alignment weight (a), cohesion weight (c), food factor (f), enemy factor (e), and inertia weight (w). It is recommended to employ high alignment and low cohesion weights to achieve optimal exploration of the search space. Conversely, high cohesion, and low alignment weights are favored for effective exploitation. Therefore, it becomes crucial to adaptively adjust these weights to strike a balance between exploration and exploitation [21, 22].

Five types of performances are assigned to the artificial dragonflies, and they are listed as follows [19, 21, 22]:

1- Separation: It is defined as the way used by dragonflies to keep themselves apart from other agents. Equation (1) is used to represent this behavior.

$$S_i = -\sum_{j=1}^{N}(X - X_j) \tag{1}$$

where X: is the present individual position, X_j: the jth nearby dragonfly's position, N: is the neighborhood's size.

2- Alignment: It is about figuring out how an agent (dragonfly) may determine its velocity (speed) in relation to the velocity vectors of nearby dragonflies. Equation (2) is used to represent the alignment process.

$$A_i = \frac{\sum_{j=1}^{N} V_j}{N} \tag{2}$$

where V_j: is the speed vector of the jth neighbor.

3- Cohesion refers to the dragonflies' tendency toward the herd center. Equation (3) defines the cohesion stage.

$$C_i = \frac{\sum_{j=1}^{N} X_j}{N} - X \tag{3}$$

4- Attraction refers to agents' desire to migrate towards food sources. Equation (4) is used to describe the *ith* agent's tendency attraction to the food source.

$$F_i = X^+ - X \tag{4}$$

where X^+: denotes the location of the food source.

5- Distraction: it is stated as a dragonfly's instinct to avoid predators. Equation (5) provides ith dragonfly distraction from predator.

$$E_i = X^- + X \tag{5}$$

with X^-: refers to the location of the predator.

Within the Dragonfly Algorithm (DA), the strategy involves utilizing the best-performing agent to update position vectors and assess the fitness of food sources. Conversely, the least effective dragonfly is tasked with updating information regarding potential threats or enemies.

This approach ensures that the algorithm converges towards the most fruitful regions of the search space while actively steering clear of less favorable areas [19].

To update the positions of dragonflies, two vectors are employed: the step vector (ΔX) and the position vector (X). The step vector, outlined in Equation (6), dictates the direction of movement for the dragonflies [19].

$$\Delta_{X_{t+1}} = (sS_i + aA_i + cC_i + fF_i + eE_i) + wX_t \tag{6}$$

where, $a, c, f,$ and e are the weighting vectors described above.

After computing the step vector, the position vector is determined using Equation (7) [19].

$$X_{t+1} = X_t + \Delta_{X_{t+1}} \tag{7}$$

with t: the number of iterations.

The Dragonfly Algorithm (DA) has demonstrated effectiveness across various optimization problems, encompassing continuous, discrete, single-objective, and multi-objective scenarios [19]. Furthermore, it has found application among numerous researchers in addressing real-world challenges spanning diverse fields, including physics, chemistry, medicine, engineering, signal processing, and robotics [23-26].

2.4. Optical properties determination

For a normal irradiance, Equation (8) gives the optical transmittance (T) of the thin layer that has been placed onto a transparent surface [27].

$$T = \frac{A_1 x}{A_2 - A_3 x + A_4 x^2} \tag{8}$$

where:

$$A_1 = 16\, n_s (n^2 + k^2) \tag{9}$$

$$A_2 = [(n+1)^2 + k^2][(n+1)(n+n_s{}^2) + k^2] \tag{10}$$

$$A_3 = [(n^2 - 1 + k^2)(n^2 - n_s{}^2 + k^2) - 2k^2(n_s{}^2 + 1)]2\cos\varphi - k[2(n^2 - n_s{}^2 + k^2) + (n_s{}^2 + 1)(k^2 - 1 + k^2)]2\sin\varphi \tag{11}$$

$$A_4 = [(n-1)^2 + k^2][(n-1)(n-n_s{}^2) + k^2] \tag{12}$$

$$\varphi = \frac{4\pi nd}{\lambda} \tag{13}$$

$$x = \exp(-\alpha\, d) \tag{14}$$

$$\alpha = \frac{4\pi k}{\lambda} \tag{15}$$

where n_s and n are the substrate and the film refractive index, respectively. d : is the thin film thickness, k: extinction coefficient, α: absorption coefficients, λ: Wavelength, φ: phase, and x: absorbance.

Furthermore, dispersion refers to the fluctuation in the refractive index of a transparent material with respect to the wavelength of light. In this scenario, the refractive index of the film rises as the wavelength decreases. Several mathematical equations have been suggested for expressing dispersion formulas. Among these, the Cauchy dispersion model is widely utilized, expressed as [27]:

$$n(\lambda) = a_1 + \frac{b_1}{\lambda^2} \tag{16}$$

where a_1, a_2, b_1 and b_2 are Cauchy dispersion model's fitting parameters.

To ascertain the thickness (d) and the optical constants (n, k, α) of the thin layer, solving complex and nonlinear equations becomes imperative. In this method, the pivotal step involves treating the task of determining the optical constants and thin film thickness as an optimization (minimization) challenge. The objective is to minimize the Root Mean Square Error (RMSE) within the measured and estimated transmittance spectra, with the cost function represented as follows:

$$RMSE = Min\ (G) \tag{17}$$

where:

$$G = \sqrt{\sum_{i=1}^{m}[T_{meas}(i) - T_{est}\ (i,\xi)]^2/\Psi} \tag{18}$$

T_{meas} and T_{est} are, respectively, experimental and estimated transmittance spectra. ξ is a vector containing the list of parameters that must be identified ($\xi = [a_1, b_1, d]$).

The transmittance vector's size is given by Ψ. This stage aims to determine the best elements of ξ in such a manner that the RMSE be as lower as feasible. The effective heuristic approach of the dragonfly algorithm [19] is used to achieve this goal.

It's important to highlight that this method delivers favorable results by splitting the transmittance spectrum into two segments. The thin film thickness is determined using the transmittance data within weak and moderate absorption ranges. Furthermore, the refractive index variation, denoted as n(λ), is estimated across the entire wavelength spectrum using the obtained values of a_1 and b_1 within this interval, applied to Equation (16) for the complete wavelength spectrum. Conversely, the second segment of the spectrum addresses the high absorption region. Here, the absorption coefficient variation (α(λ)) is determined utilizing the Swanepoel approximation [28] after substituting the previously calculated values of n and d, as follows:

$$T_\alpha = \sqrt{T_M T_m} \tag{19}$$

$$G = \frac{128n^4 n_s^2}{T_\alpha^2} + n^2(n^2-1)^2(n_s^2-1)^2 + (n^2-1)^2(n^2-n_s^2)^2 \tag{20}$$

$$x = \frac{\left\{G - \left[G^2 - (n^2-1)^6(n^2-n_s^4)^2\right]^{1/2}\right\}^{1/2}}{(n-1)^3(n-n_s^2)} \tag{21}$$

$$\alpha = \frac{-\log(x)}{d} \tag{22}$$

Upper and lower tangent envelopes are represented by T_M and T_m in Equation (19). Following that, an extrapolation step will be established to compute the absorption coefficient variation $\alpha(\lambda)$ throughout the whole wavelength range. Finally, using Equation (15), the extinction coefficient variation $k(\lambda)$ is calculated.

3. Results and discussion

3.1. XRD analysis

X-ray diffraction patterns of ZnO and Mn-doped ZnO are shown in Figure 1. One can see from the XRD data that our samples have a single phase. For the non-annealed one, five peaks that belong to Zn metal (ICCD No.001-1238) were noticed; the corresponding planes of those peaks are (002), (100), (101), (102), and (110), respectively. No other peaks indicate the existence of ZnO, which means the oxidation of Zn occurs after the heat treatment. The main reason for the ZnO oxide phase's disappearance is the subdivision of ZnO molecules during the evaporation process, giving Zn atoms and oxygen gas. This last will be pumped majoritively by the pumping group, which prevents the ZnO phase creation [29]. Concerning the annealed samples, analysis based on the powder diffraction standard card (ICCD No.001-1136) reveals distinct peaks. Those

with higher intensities, such as those corresponding to the planes (100), (002), and (101), as well as peaks with lower intensities like (102), (110), (103), and (112), collectively signify the presence of the hexagonal wurtzite structure characteristic of ZnO. This observation suggests that the ZnO mesh was disturbed when the Mn concentration was raised. It's likely that throughout the annealing process, Mn atoms operate as barriers (traps or dispersion centers) that prevent ZnO from developing, causing the film's crystallinity to deteriorate and the peak's intensity to drop. Many research works [30, 31] have reported on this fact. In addition, the examination of the XRD patterns reveals that the peaks of Mn-doped films are somewhat displaced to a lower angle than those of the undoped ZnO films. The structure's micro-strain from vacancies, stacking faults, and interstitials may have caused this shift [32]. Nevertheless, the absence of peaks characteristic of manganese (Mn) indicates that Mn has likely replaced zinc (Zn) sites within the wurtzite structure without altering its fundamental characteristics.
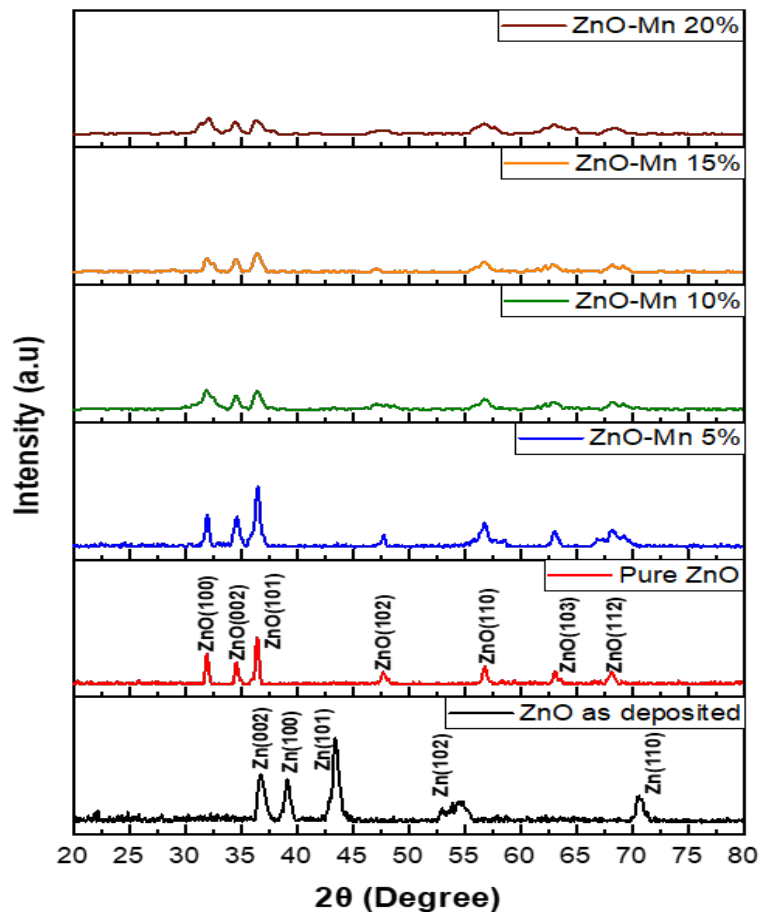

Fig. 1. X- ray diffraction patterns of pure and doped zinc oxide films.

Identifying any modifications in these structural characteristics is advantageous to gain insights into the alterations in the physical properties of our layers. The lattice parameters were established using [33]:

$$a = \frac{\lambda}{sin\theta_{hkl} \sqrt{3}} \tag{23}$$

$$c = \frac{\lambda}{sin\theta_{hkl}} \tag{24}$$

In this equation, λ represents the wavelength of the X-ray, θ_{hkl} denotes the diffraction angle, and hkl refers to the Miller indices.

The formulas used to calculate the crystallite size D, microstrain τ, and dislocation density δ are as follows [34]:

$$D = \frac{0.9\lambda}{FWHM cos\theta_{hkl}} \tag{25}$$

$$\tau = \frac{FWHM}{4 tan\theta_{hkl}} \tag{26}$$

$$\delta = \frac{1}{D^2} \tag{27}$$

The lattice parameters of our samples barely changed after adding different amounts of Mn; this phenomenon can be explained by the similarity in the radii of manganese (Mn) ions (0.66 Å) and zinc (Zn) ions (0.60 Å), facilitating the straightforward substitution of Zn atoms with Mn atoms. The 'c' axes values variation began with an unnoticed increase at 5 wt.-% Mn doping, then it increases with Mn concentration rise (Figure 2a). All 'c' values exceed the value of theoretical pure zinc oxide (c_0= 0.5205 nm). This implies that ZnO sheets experience compressive forces along the c-axis [35]. In Figure 2b, the full width at half-maximum (FWHM) of the thin films increases as the quantity of Mn incorporated rises. This augmentation in FWHM is ascribed to the reduction in crystallite size induced by doping. The lowest FWHM value is observed for pure ZnO films, suggesting the highest level of crystallinity. The widening of the diffraction peaks is a results of the increase of strain, lattice defects, and dislocation density, which leads to a reduction in crystallite size. This highlights the influence of the incorporation of Mn atoms [36].

Table 1. Crystallites size D, FWHM, micro strain τ, dislocation density δ and lattice parameters.

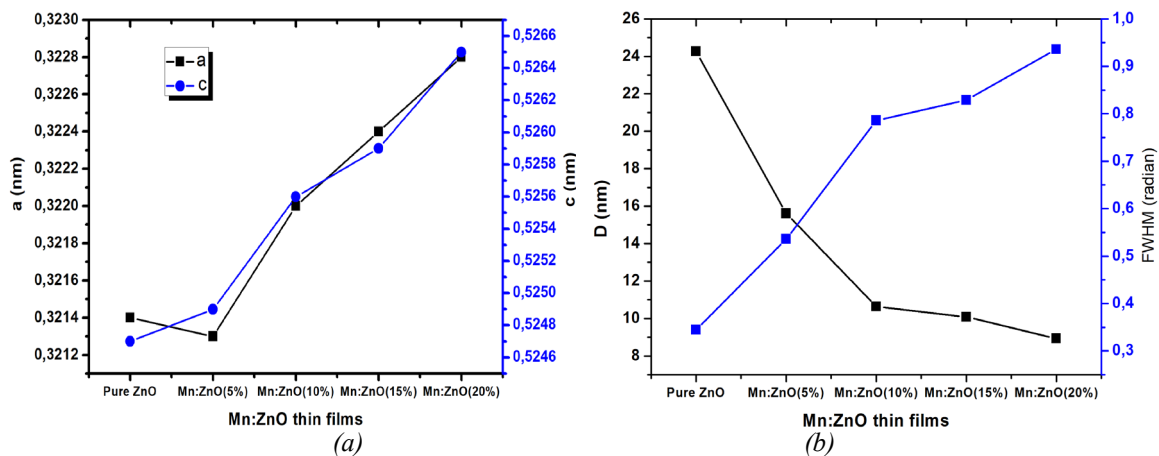|	D (nm)	FWHM (rad)	τ	δ (nm^{-2})	a (nm)	c (nm)
Pure ZnO	24.26	0.3447	0.0046	0.0017	0.3214	0.5247
Mn:ZnO(5 wt.-%)	15.61	0.5359	0.0071	0.0041	0.3213	0.5249
Mn:ZnO(10 wt.-%)	10.64	0.7855	0.0104	0.0088	0.3220	0.5256
Mn:ZnO(15 wt.-%)	10.08	0.8290	0.0110	0.0098	0.3224	0.5259
Mn:ZnO(20 wt.-%)	8.93	0.9361	0.0125	0.0125	0.3228	0.5265

Fig. 2. Variation of a) lattice parameters 'a' and 'c' b) FWHM, crystallites size D of ZnO mesh as a function of Mn content.

3.2. Raman analysis

The Raman scattering technique was employed to analyze the vibrational characteristics of the hexagonal wurtzite structure present in both pure and doped zinc oxide layers. The findings are illustrated in Figure 3. It is evident that all samples exhibit the A_1(LO) vibration mode, with frequencies around Σ 572 cm^{-1} for Mn:ZnO films and 569 cm^{-1} for pure zinc oxide. The A_1 longitudinal optical phonon in the wurtzite structure of zinc oxide is polarized parallel to the c-axis; this vibration mode gives the oxidation state of the films. Within doped films, the introduction of manganese atoms occurs within the zinc oxide host lattice. Conversely, in pure zinc oxide films, the process of incomplete oxidation leads to the integration of zinc atoms into the zinc oxide lattice, thereby inducing self-doping [37].

The incorporation of a dopant into the mesh may result in the appearance of local vibration modes (LVM) in the Raman spectra. The disruption of the crystal's translational symmetry by impurity-induced defects is one proposed physical basis for understanding LVM. Due to the wave vector's loss of conservation, phonon scattering with wave vectors far from the Brillouin zone occurs [38]. Because of the surplus of Mn atoms within the ZnO matrix, LVM modes can be found clearly for Mn:ZnO (15 wt.-% and 20 wt.-% Mn) samples. However, for the pure ZnO films, the disappearance of this vibration mode can be noticed. The rest of the detected peaks for the Mn:ZnO films (887 and 847 cm^{-1}) may be attributed to the molecules with Mn [39]. A_1(LO)+E_2(Low) mode for the high doped films is related to poly-phonon scattering [40]. Vibration modes at 706 cm^{-1} and 900 cm^{-1} for pure ZnO samples are given A_1 symmetry of ZnO processes that combine LA+TO phonons [41].
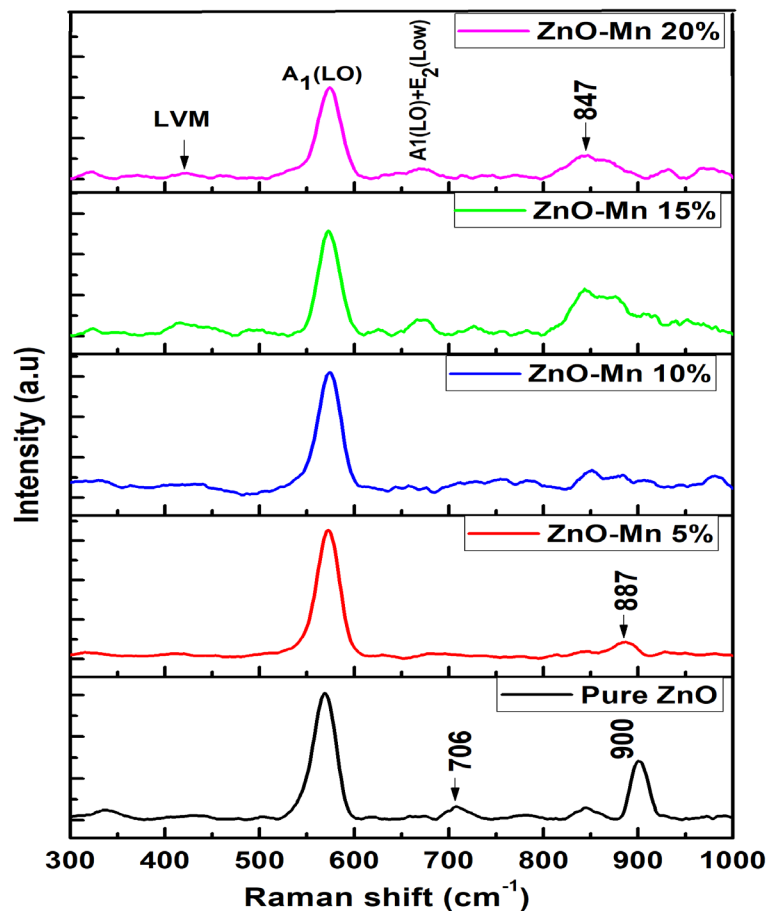

Fig. 3. Raman shift for pure and doped zinc oxide films.

3.3. Surface morphology

SEM was utilized to analyze the surface morphology of the non-doped and doped layers. The outcomes are depicted in Figure 4 (a-e). It is clear from the electron micrographs that all substrates are well covered with the thin layer, showing a non-uniform surface morphology. Pure ZnO film shows spherical particles agglomerations spread unevenly onto the substrate with an average size of 5.36 μm. It is apparent that Mn doping modified the morphology to become more homogenous; the agglomerations are closely packed, with grain size noticeably smaller than the non-doped films. Due to the impact nature of ZnO clusters, pits and holes that signify the escape of gases during thermal evaporation were observed. The chemical composition was analyzed using EDX. It confirms the existence of Zn, Mn, and O atoms. There are pics indicating the Si corresponding to the glass substrate.
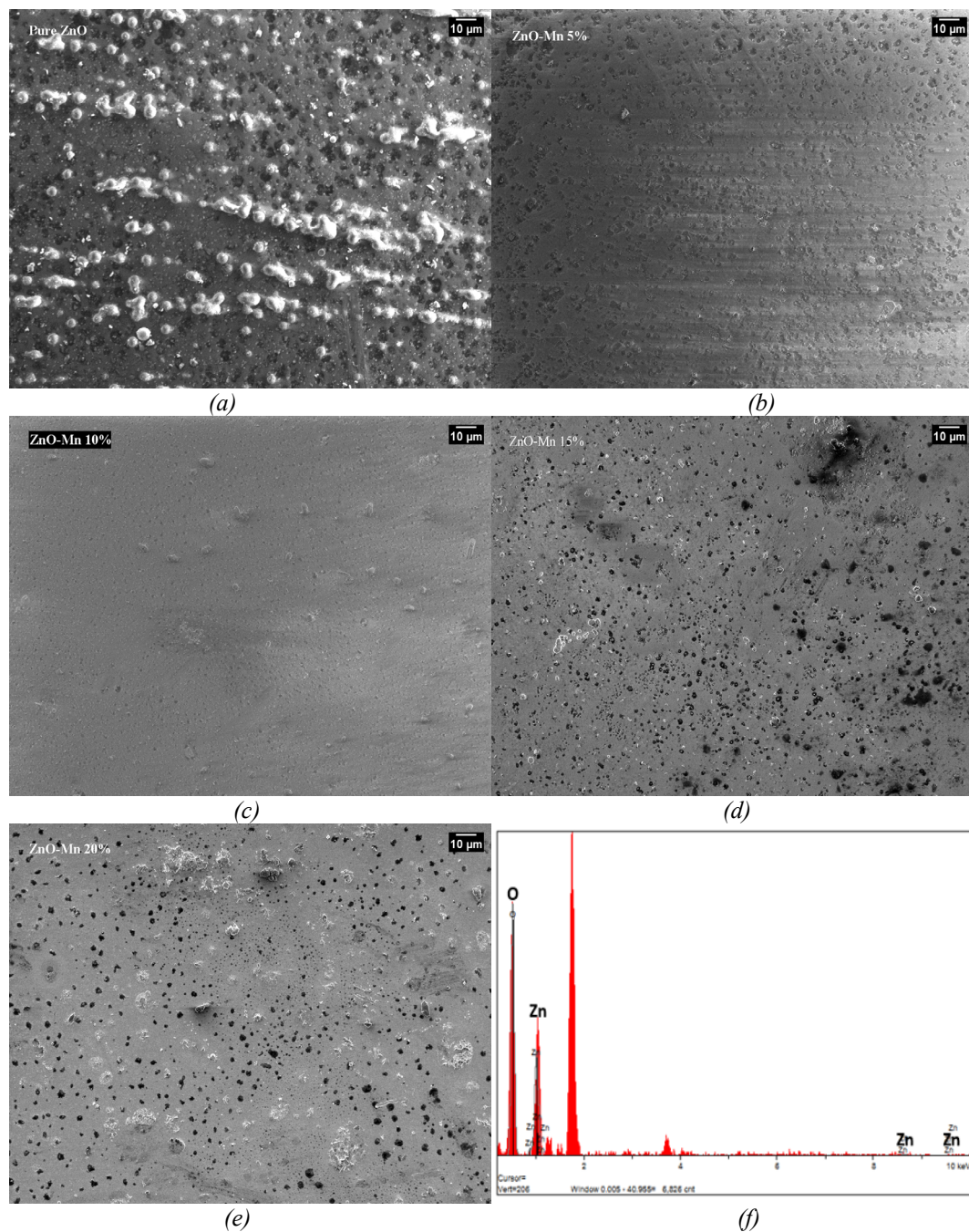

Fig. 4. SEM images of layers: (a) pure ZnO, (b) ZnO-Mn 5%, (c) ZnO-Mn 10%, (d) ZnO-Mn 15%, (e) ZnO-Mn 20% and (f) EDX results for 20% doping.

3.4. Optical properties

The optical transmission spectra of our samples were recorded in the wavelength region of 250-800 nm in Figure 5. The thickness of the layers is calculated using the DA algorithm, which is about 120 nm. Each sample demonstrates transparency within the visible spectrum, with the pure ZnO film exhibiting the highest transmission at 83.1%.
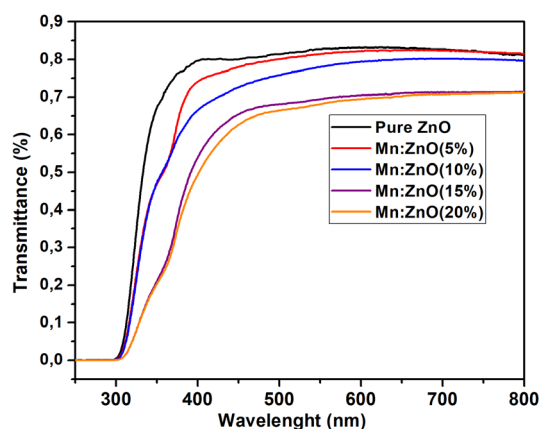

Fig. 5. Spectra depicting the optical transmittance of both pure and doped zinc oxide films.

The increase in Mn percentage causes a decrease in optical transmission, up to 69.5% for Mn:ZnO (20 wt.-%Mn), and this might be due to the light loss caused by oxygen vacancies and diffusion at grain boundaries [42]. The decline in transmittance observed as the percentage of Mn increases is attributed to the reduction in optical diffusion [31], which is linked to a decrease in the grain size and to the increase in the density of grain boundaries. These results are in perfect adequation with the XRD analysis section, and the grain size decreases with the manganese amount increase.

The consistency between the measured and estimated transmittance is apparent for all samples. As an example, the case of the sample with 20 wt.-% Mn doping is detailed. Figure 6 confirms that the dragonfly algorithm successfully determined the optical parameters of our films, the measured transmittance and the estimated one are almost identical, and the root mean square estimated by Equation (18) is around 0.00145.

The transmittance spectrum of Mn-doped ZnO thin films has been analyzed using the DA algorithm to showcase the efficacy of this methodology, for the sample containing a 20 wt.-% Mn doping concentrate, a thorough explanation will be provided with illustrations. Additionally, as mentioned in Section (2-4), the user can adjust several control settings for the DA algorithm. These parameters were empirically selected for this study using a trial-and-error methodology. This indicates that the DA algorithm's effectiveness has been evaluated for a number of values, and only the best ones are chosen. Table 2 in this paper provides an overview of the Dragonfly Algorithm's configuration parameters.

Table 2. Setting parameters of DA.

Parameter	Value
Population size	80
Number of iterations	200
Dimension	5
Separation weight	0.1
Alignment weight	0.1
Cohesion weight	0.7
Food factor	1
Enemies factor	1

The variation ranges of each parameter are depicted in Table 3.

Table 3. The variation ranges of every parameter.

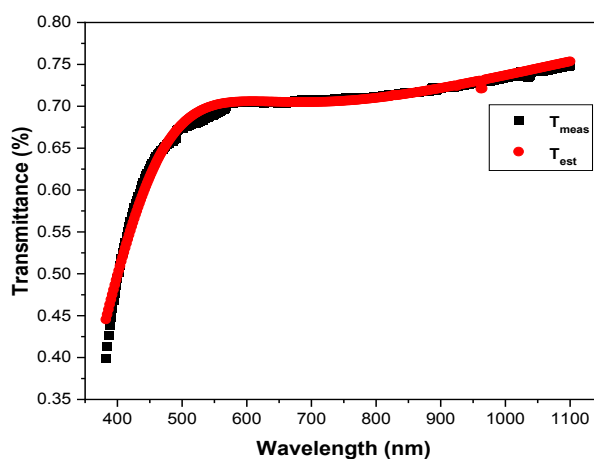| Parameter	variation range
α_1	$[1 - 3]$
β_1	$[10^4 - 10^6]$
α_2	$[10^{-5} - 10^{-2}]$
β_2	$[10^3 - 10^5]$
D	$[60 - 400]$

Fig. 6. Measured and estimated transmittance for 20wt.-% Mn doped ZnO.

For instance, the obtained optimal parameters and reached RMSE for the Mn:ZnO (20wt.-%) are given in Table 4.

Table 4. The obtained results for Mn:ZnO (20wt.-%).

Parameters	$\alpha_1{}^*$	$\beta_1{}^*$	$\alpha_2{}^*$	$\beta_2{}^*$	d^*	*RMSE*
Value	2.05	$7.17 \times 10^{+04}$	3.77×10^{-4}	$1.64 \times 10^{+4}$	105	1.45×10^{-03}

Additionally, the results in Table 4 clearly illustrate the DA algorithm's outstanding performance in precisely determining the optical film thickness and Cauchy dispersion parameters. The low RMSE value of 1.45×10^{-03} confirms the high accuracy of the approach.

The refractive index can be rewritten as follows using the Table 4 parameters:

$$n(\lambda) = 2.05 + \frac{7.17 \times 10^{+4}}{\lambda^2} \tag{28}$$

The entire wavelength range can be extrapolated using this equation to determine n. The estimated values of n are shown in Figure 7.
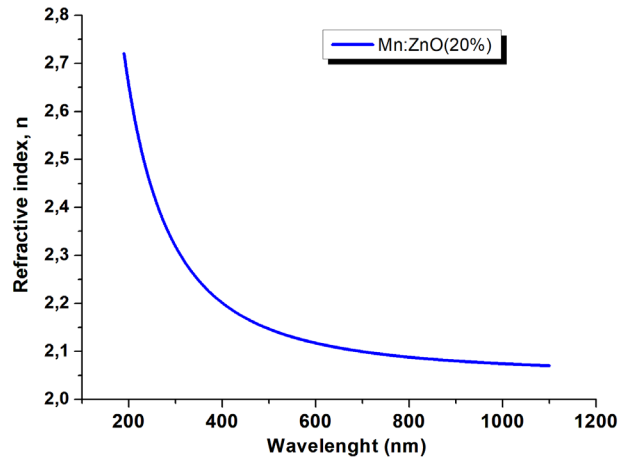
Fig. 7. The dispersion of refractive index n for the whole wavelength range.

The determination of the static refractive index involves setting the variable of the Cauchy relation model in Equation (28) to "approaches infinity". The measured values for pure and manganese doped zinc oxide samples (5, 10, 15 and 20 wt.-%) are 1.76, 1.90, 1.92, 2.112 and 2.17, respectively. With a rise in Mn doping, the refractive index at a wavelength of 600 nm is determined to be 1.785, 1.925, 1.952, 2.142, and 2.197. A rise in the refractive index was observed with an increase in the amount of manganese. Few studies in the existing literature have investigated the impact of manganese concentration on the refractive index of zinc oxide. However, the same results were reported by Shaaban et al. [43], which was explained by the increase of polarization resulting from Mn incorporation. P. Singh and R. Kumar [44] reported similar results, but for Er-doped ZnO films, they found that the concentration of erbium increases the refractive index of the material and because of its power of polarizability. Erbium ions (Er^{3+}) have the most empty outer orbital will bring the material back towards linear polarizability, which increases the refractive index of the material. The same can be said for Mn and its influence on Mn:ZnO thin films. For the calculated extinction coefficient based on the values of the absorption coefficient α, using Equation (22). The values depicted in Table 5 are practically the same for the layers not doped and doped at 5 and 10 wt.-%. However, the value of k increases when the doping becomes important (15 and 20 wt.-%).

As depicted in Figure 8, the graphs illustrate plots of $(\alpha h\upsilon)^2$ against $(h\upsilon)$. The optical band gap of the thin films was determined by extrapolating the linear portion of the curve to reach $(\alpha h\upsilon)^2 = 0$. This calculation is performed using the following formula [45, 46]:

$$\alpha h\upsilon = A \sqrt{h\upsilon - Eg}$$ (29)

The optical band gap of the zinc oxide film measures 3.95 eV, showing a slight reduction to 3.79 eV after Mn doping, reaching this value at 20 wt.-% Mn. The decrease in band gap upon doping ZnO with varying concentrations of Mn is theoretically linked to the exchange interaction between the electrons of the sp orbital of ZnO and the Mn d orbital [47]. On the other hand, many researchers explain the change in band gap E_g by the strains in semiconductor films, it can be explained by the following empirical expression [48]:

$$E_g = 3.28 - 0.045\varepsilon_z$$ (30)

The strains (ε_z) values can be calculated based on c-axis values determined in the XRD section and using this formula [49]:

$$\varepsilon_z = \left(\frac{c - c_0}{c_c}\right)$$ (31)

The films band gap will increase for negative strain and decrease for positive strain; according to Equation (32), εz values are +0.0080, +0.0084, +0.0098,, 0.0103 and 0.0115 for pure ZnO and Mn:ZnO films (5, 10, 15 and 20 wt.-%), respectively. Since ε_z has positive values in our situation, which conduct to the Eg rising (Figure 9).

Table 5. The parameters examined include the band gap (Eg), transmittance (T), refractive index (n), and extinction coefficient (k) of both the non-doped and doped samples.

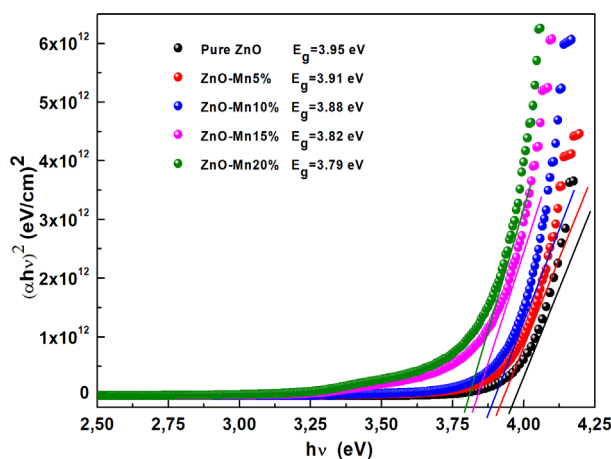|	Eg (eV)	T (%) (λ=600)	N (λ=600)	n_0(static)	k (λ=600)	k_0(static)
Pure ZnO	3.95	83.1	1.785	1.760	0.013	0.039
Mn:ZnO (5wt.-%)	3.91	82.2	1.925	1.900	0.018	0.040
Mn:ZnO(10wt.-%)	3.88	79.5	1.952	1.920	0.015	0.035
Mn:ZnO (15wt.-%)	3.82	70.4	2.142	2.112	0.072	0.084
Mn:ZnO (20wt.-%)	3.79	69.5	2.197	2.170	0.064	0.057

Fig. 8. The plots of $(\alpha h\nu)^2$ as function of photon energy of non-doped and Mn-doped zinc oxide thin films.

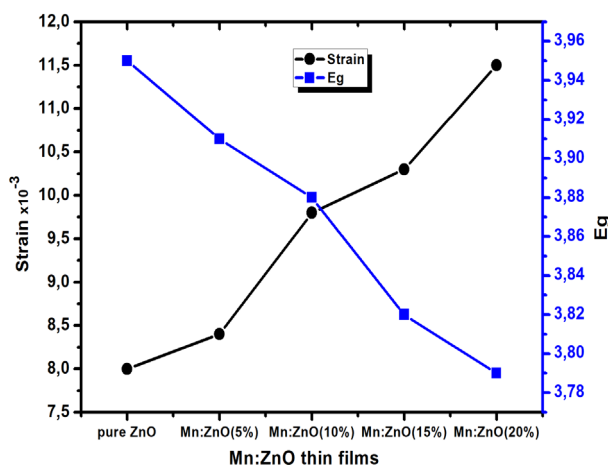*Fig. 9. The changes in band gap (Eg) and strain (ε_z) with respect to the concentration of Mn doping are examined in this study.*

4. Conclusion

This study meticulously explores the structural and optical characteristics of Mn-doped ZnO thin films across varying concentrations of Mn doping. The samples were made using the rapid thermal evaporation of ZnO and Mn particles in combination. Following annealing, Mn:ZnO layers form in the hexagonal wurtzite phase with an increase in c-axis and crystallite size decrease, according to XRD studies. Raman measurements have shown the desapearance of the combined vibrations modes LA+TO after doping with Mn and the appearance of $A_1(LO)+E_2(Low)$ mode for the high doping samples (15 and 20 %).

The average optical transmittance for the annealed Mn:ZnO layers was decreased with Mn doping concentration increase from 83.1 to 69.5%. For the first time, the Dragonfly Algorithm was used to correctly identify and calculate the optical constants n, α, k and the thickness d using only the transmittance spectra. Furthermore, the energy band gap Eg was calculated for various Mn doping levels. According to the obtained data, Eg reduces from 3.95 to 3.79 eV as Mn doping concentration increases from 0 to 20 wt.-%.

References

[1] H. Kim, A. C. Gilmore, A. Pique, J. Horwitz, H. Mattoussi, H. Murata et al., " Journal of applied physics, vol. 86, pp. 6451-6461, 1999; https://doi.org/10.1063/1.371708

[2] Z. Chen, W. Li, R. Li, Y. Zhang, G. Xu, H. Cheng, Langmuir, vol. 29, pp. 13836-13842, 2013; https://doi.org/10.1021/la4033282

[3] S. K. Kim, K. M. Kim, D. S. Jeong, W. Jeon, K. J. Yoon, C. S. Hwang, Journal of Materials Research, vol. 28, pp. 313-325, 2013; https://doi.org/10.1557/jmr.2012.231

[4] M. Becker, R. Hamann, A. Polity, B. K. Meyer, Thin Solid Films, vol. 553, pp. 26-29, 2014; https://doi.org/10.1016/j.tsf.2013.11.030

[5] F. Lekoui, R. Amrani, S. Hassani, E. Garoudja, W. Filali, S. Oussalah et al., Zeitschrift für Naturforschung A, 2023; https://doi.org/10.1515/zna-2023-0046

[6] F. Lekoui, R. Amrani, S. Hassani, Elyes Garoudja, Walid Filali, M. Ouchabane et al, Optical Materials, vol. 150, p. 115151, 2024; https://doi.org/10.1016/j.optmat.2024.115151

[7] A. Mallick, S. Ghosh, D. Basak, Materials Science in Semiconductor Processing, vol. 119, p. 105240, 2020; https://doi.org/10.1016/j.mssp.2020.105240

[8] F. Lekoui, R. Amrani, W. Filali, E. Garoudja, L. Sebih, I. E. Bakouk et al., Optical Materials, vol. 118, p. 111236, 2021; https://doi.org/10.1016/j.optmat.2021.111236

[9] S. V. Bhat, F. Deepak, Solid State Communications, vol. 135, pp. 345-347, 2005; https://doi.org/10.1016/j.ssc.2005.05.051

[10] A. Vincze, J. Bruncko, M. Michalka, D. Figura, Open Physics, vol. 5, pp. 385-397, 2007; https://doi.org/10.2478/s11534-007-0027-4

[11] Kamil, A. A., Bakr, N. A., Mubarak, T. H., Al-Zanganawee, Journal of Ovonic Research, 18(3), 431-442, 2022; https://doi.org/10.15251/JOR.2022.183.431

[12] Zaouche, C., Dahbi, L., Benramache, S., Harouache, A., Derouiche, Y., Kharroubi, M., Alkhojah, H. M., Journal of Ovonic Research, 19(2), 2023; https://doi.org/10.15251/JOR.2023.192.197

[13] A. Ashour, M. Kaid, N. El-Sayed, A. Ibrahim, Applied Surface Science, vol. 252, pp. 7844-7848, 2006; https://doi.org/10.1016/j.apsusc.2005.09.048

[14] S. Faÿ, J. Steinhauser, S. Nicolay, C. Ballif, Thin Solid Films, vol. 518, pp. 2961-2966, 2010; https://doi.org/10.1016/j.tsf.2009.09.189

[15] J. Elanchezhiyan, P. Bhuvana, N. Gopalakrishnan, A. Thamizhavel, T. Balasubramanian, Zeitschrift für Naturforschung A, 63 (9), PP. 585-590, 2008; https://doi.org/10.1515/zna-2008-0909

[16] X. Liu, R. Hao, Q. Zhao, F. Chang, Y. Li, K. Gu et al., (2018), Zeitschrift für Naturforschung

A, 73 (10), pp. 957-964, 2018; https://doi.org/10.1515/zna-2018-0177

[17] S. Baturay, O. Bicer, S. Yigit Gezgin, I. Candan, H. Budak Gumgum, H. Kilic, Zeitschrift für Naturforschung A, 78(6), pp. 563-578, 2023; https://doi.org/10.1515/zna-2023-0015

[18] A. Zaier, A. Meftah, A. Jaber, A. Abdelaziz, M. Aida, Journal of King Saud University-Science, vol. 27, pp. 356-360, 2015; https://doi.org/10.1016/j.jksus.2015.04.007

[19] S. Mirjalili, Neural computing and applications, vol. 27, pp. 1053-1073, 2016; https://doi.org/10.1007/s00521-015-1920-1

[20] E. Garoudja, R. Amrani, W. Filali, F. Lekoui, S. Oussalah, Y. Cuminal et al., Optik, vol. 241, p. 167030, 2021; https://doi.org/10.1016/j.ijleo.2021.167030

[21] W. Filali, R. Amrani, E. Garoudja, S. Oussalah, F. Lekoui, Z. Oukerimi et al., Superlattices and Microstructures, vol. 160, p. 107085, 2021; https://doi.org/10.1016/j.spmi.2021.107085

[22] Y. Meraihi, A. Ramdane-Cherif, D. Acheli, M. Mahseur, Neural Computing and Applications, vol. 32, pp. 16625-16646, 2020; https://doi.org/10.1007/s00521-020-04866-y

[23] D. Poelman, P. F. Smet, Journal of Physics D: Applied Physics, vol. 36, p. 1850, 2003; https://doi.org/10.1088/0022-3727/36/15/316

[24] C. M. Rahman, T. A. Rashid, A. Alsadoon, N. Bacanin, P. Fattah, S. Mirjalili, Evolutionary Intelligence, vol. 16, pp. 1-21, 2023; https://doi.org/10.36227/techrxiv.11811768.v4

[25] M. Mafarja, A. A. Heidari, H. Faris, S. Mirjalili, I. Aljarah, Nature-Inspired Optimizers: Theories, Literature Reviews and Applications, pp. 47-67, 2020; https://doi.org/10.1007/978-3-030-12127-3_4

[26] Yıldız, Betül Sultan, Yıldız, Ali Rıza, Materials Testing, vol. 61, no. 8, pp. 744-748, 2019; https://doi.org/10.3139/120.111379

[27] Z.-H. Ruan, Y. Yuan, X.-X. Zhang, Y. Shuai, H.-P. Tan, Solar Energy, vol. 127, pp. 147-158, 2016; https://doi.org/10.1016/j.solener.2016.01.027

[28] R. Swanepoel, Journal of Physics E: Scientific Instruments, vol. 16, p. 1214, 1983; https://doi.org/10.1088/0022-3735/16/12/023

[29] F. Lekoui, S. Hassani, E. Garoudja, R. Amrani, W. Filali, O. Sifi, S. Oussalah, Rev. Mex. Fís., vol. 69, p. 051005, 2023; https://doi.org/10.31349/RevMexFis.69.051005

[30] S. Ahmed, Results in physics, vol. 7, pp. 604-610, 2017; https://doi.org/10.1016/j.rinp.2017.01.018

[31] A. López-Suárez, D. Acosta, C. Magaña, F. Hernández, Journal of Materials Science: Materials in Electronics, vol. 31, pp. 7389-7397, 2020; https://doi.org/10.1007/s10854-019-02830-8

[32] R. Baghdad, B. Kharroubi, A. Abdiche, M. Bousmaha, M. Bezzerrouk, A. Zeinert et al., Superlattices and Microstructures, vol. 52, pp. 711-721, 2012; https://doi.org/10.1016/j.spmi.2012.06.023

[33] M. Boshta, M. Abou-Helal, D. Ghoneim, N. Mohsen, R. Zaghlool, Surface and Coatings Technology, vol. 205, pp. 271-274, 2010; https://doi.org/10.1016/j.surfcoat.2010.06.039

[34] J. Li, D. Yang, X. Zhu, H. Sun, X. Gao, P. Wangyang et al., Journal of Sol-Gel Science and Technology, vol. 82, pp. 563-568, 2017; https://doi.org/10.1007/s10971-017-4335-x

[35] M. Mekhnache, A. Drici, L. S. Hamideche, H. Benzarouk, A. Amara, L. Cattin et al., Superlattices and Microstructures, vol. 49, pp. 510-518, 2011; https://doi.org/10.1016/j.spmi.2011.02.002

[36] S. Hemathangam, G. Thanapathy, S. Muthukumaran, Journal of Materials Science: Materials in Electronics, vol. 27, pp. 1791-1798, 2016; https://doi.org/10.1007/s10854-015-3955-6

[37] S. Khosravi-Gandomani, R. Yousefi, F. Jamali-Sheini, N. M. Huang, Ceramics international, vol. 40, pp. 7957-7963, 2014; https://doi.org/10.1016/j.ceramint.2013.12.145

[38] J. Li, D. Yang, X. Zhu, Aip Advances, vol. 7, 2017; https://doi.org/10.1063/1.4985753

[39] J. Wang, G. Huang, X. Zhong, L. Sun, Y. Zhou, E. Liu, Applied Physics Letters, vol. 88, 2006; https://doi.org/10.1063/1.2208564

[40] K. Hamidian, M. Sarani, M. Barani, F. Khakbaz, Arabian Journal of Chemistry, vol. 15, p. 103792, 2022; https://doi.org/10.1016/j.arabjc.2022.103792

[41] R. Cuscó, E. Alarcón-Lladó, J. Ibáñez, L. Artús, J. Jiménez, B. Wang et al., Physical Review B, vol. 75, p. 165202, 2007; https://doi.org/10.1103/PhysRevB.75.165202

[42] H. K. Yadav, K. Sreenivas, V. Gupta, Journal of Applied Physics, vol. 99, 2006; https://doi.org/10.1063/1.2188083

[43] E. Shaaban, M. El-Hagary, M. Emam-Ismail, A. Matar, I. Yahia, Materials Science and Engineering: B, vol. 178, pp. 183-189, 2013; https://doi.org/10.1016/j.mseb.2012.11.005

[44] P. Singh, R. Kumar, Optik, vol. 246, p. 167829, 2021; https://doi.org/10.1016/j.ijleo.2021.167829

[45] R. Amrani, E. Garoudja, F. Lekoui, W. Filali, H. Neggaz, Y. A. Djebeli et al., Bulletin of Materials Science, vol. 46, p. 8, 2023; https://doi.org/10.1007/s12034-022-02845-8

[46] D. Grine, H. Akkari, P. Fernández, T. Mekhalif, S. Hassani, F. Lekoui, Physica Status Solidi A, vol. 219, p. 2200036, 2022; https://doi.org/10.1002/pssa.202200036

[47] M. Shatnawi, A. Alsmadi, I. Bsoul, B. Salameh, M. Mathai, G. Alnawashi et al., Results in Physics, vol. 6, pp. 1064-1071, 2016; https://doi.org/10.1016/j.rinp.2016.11.041

[48] L. Peng, L. Fang, X. Yang, Y. Li, Q. Huang, F. Wu et al., Journal of Alloys and Compounds, vol. 484, pp. 575-579, 2009; https://doi.org/10.1016/j.jallcom.2009.04.139

[49] H. Chen, J. Ding, W. Guo, F. Shi and Y. Li, Applied surface science, vol. 258, pp. 9913-9917, 2012; https://doi.org/10.1016/j.apsusc.2012.06.050